Journal of Zhejiang University-SCIENCE A (Applied Physics & Engineering)
ISSN 1673-565X (Print); ISSN 1862-1775 (Online)
www.jzus.zju.edu.cn; www.springerlink.com
E-mail: jzus@zju.edu.cn

A pore-scale numerical investigation of the effect of pore characteristics on flow properties in soils*

Guang-yao LI[1,2], Sheng DAI[2], Liang-tong ZHAN[†‡1], Yun-min CHEN[1]

[1]*MOE Key Laboratory of Soft Soils and Environmental Engineering, Zhejiang University, Hangzhou 310058, China*

[2]*School of Civil and Environmental Engineering, Georgia Institute of Technology, Atlanta 30332 GA, USA*

[†]E-mail: zhanlt@zju.edu.cn

Received June 15, 2019; Revision accepted Oct. 9, 2019; Crosschecked Nov. 7, 2019

Abstract: Flow properties of soils can impact a wide range of geotechnical, agricultural, and geophysical processes. Few studies focus on the physical understanding of how pore characteristics can affect flow properties in soils. In this paper, pore network modeling is utilized to investigate intrinsic permeability, water pressure distributions, flow patterns, and critical flow paths in soils with pores varying in size, connectivity, and anisotropy. The results show that increased mean diameter, decreased standard deviation, and increased coordination number of the pores can lead to an increase in intrinsic permeability in soils. Non-uniform water pressure and flow rate distribution will more likely occur in soils with a larger pore size variability. A higher coordination number mitigates the pressure localization but slightly exacerbates non-uniform flow. With the increase in the coefficient of variation (COV) of pore diameters, the percolation path becomes more tortuous and carries more flow. When COV increases from 0 (homogeneous) to 1 (large pore size variability), the tortuosity increases from 1.00 to ~1.71 and the flux carried by the percolation path in soils increases from 2.0% to 7.8%. Pronounced preferential flows may take place in soils with uniformly distributed pore sizes, in which the percolation path can carry as much as 9.2% of the total flux. The anisotropy in pore throat sizes also increases the flow tortuosity and the fraction of flux carried by the percolation path. The permeability anisotropy K_h/K_v increases linearly as the pore throat size anisotropy μ_{dh}/μ_{dv} increases logarithmically. These results provide insight for designing soil barriers for either uniform flows or exacerbated preferential flow for fast transport.

Key words: Pore network modeling; Intrinsic permeability; Flow properties; Pore characteristics
https://doi.org/10.1631/jzus.A1900255 **CLC number:** TU4

1 Introduction

Flow properties of soils can impact a wide range of geotechnical, agricultural, and geophysical processes, such as slope stability (Shao et al., 2015), contaminant transport (Ghodrati et al., 1999), groundwater recharge (Bianchi et al., 2011), soil/structure interaction (Ng et al., 2017, 2018; Li et al., 2018; van Dijk, 2018; Yan et al., 2018), resource recovery efficiency (Maitland, 2000; Sun et al., 2018), and the performance of landfill covers (Zhan et al., 2017b). For example, the management of municipal solid waste is a major environmental challenge facing the world today. Landfilling is the dominant option for waste disposal in many developed and developing countries (Laner et al., 2012; Zhan et al., 2017a). As one of the important components of landfills, final covers minimize percolation into the underlying waste and limit the emission of landfill gases. The performance of final covers is strongly related

‡ Corresponding author

* Project supported by the National Science Fund for Distinguished Young Scholars (No. 51625805), China, the Program of China Scholarships Council (No. 201706320096), the Zhejiang Provincial Key Research Project of China (No. 2015C03021), the Engineering Research Center Program of the US National Science Foundation (No. EEC-1449501), and the US DOE/NETL Gas Hydrate Research Program

ORCID: Guang-yao LI, https://orcid.org/0000-0002-9724-6044

to their flow properties such as non-uniform and rapid transport of water or solutes. Thus, knowledge concerning the transport processes in covered materials is required.

Flow properties of saturated porous media are inherently controlled by pore characteristics, such as pore size distribution, pore shape, and topology. More complicated mechanisms, e.g. hysteresis and wettability alteration, affect the flow when the porous media become unsaturated (Morrow, 1975; van Genuchten, 1980). Defined by grain size distribution and formation history, pores in natural sediments vary widely in size, shape, connectivity, and spatial distribution, leading to several scales of heterogeneity, layering, and hydrophobicity. Many studies focus on transport processes in soils with apparent inhomogeneity of macro-pores, cracks, earthworm burrows, or vegetation root channels (Šimůnek et al., 2003; Gerke, 2006; Allaire et al., 2009). Theoretical descriptions of water transport by considering the coexistence of inter-aggregate pores and intra-aggregate pores have been proposed (Gerke and van Genuchten, 1996; Ross and Smettem, 2000; Hunt et al., 2013; Hirashima et al., 2014). Experimentally, dye tracers combined with image analysis have been used to visualize flow processes in various types of soils at both laboratory and field scales (Andreini and Steenhuis, 1990; Flury and Flühler, 1994; Allaire-Leung et al., 2000; Öhrström et al., 2004; Weiler and Flühler, 2004). Relevant results play an important role in engineering applications, but there are still challenges, such as the limited resolution of imaging techniques, in capturing pore-scale phenomena (Bultreys et al., 2015, 2016, 2018; Singh et al., 2017; Scanziani et al., 2018). Owing to the complexity of pore-scale geometries, severe practical difficulties and large uncertainties are found at dimensions larger than the representative elementary volume (REV) scale for highly heterogeneous pore media. Therefore, knowing the pore-scale transport processes contributes to improving the understanding of the behavior of soils at larger scales.

Over the past decades, theoretical, experimental, and numerical approaches have been proposed and developed to study pore-scale transport processes through soils. Flow experiments combined with X-ray, scanning electron microscopy (SEM), and transmission electron microscopy (TEM) techniques can provide direct and valuable information, but the results are usually sensitive to material composition and sample preparation. Analytical solutions are usually based on the assumption of homogeneous properties, leading to limited practical relevance (Xiong et al., 2016). In recent years, pore-scale simulations have shown many advantages in the determination of transport properties in porous media, e.g. the lattice Boltzmann method, the coupled computational fluid dynamics and discrete element method (CFD-DEM) model, and the pore network modeling. Among these methods, pore network modeling is the least time-consuming due to the inherent simplifications of void space. It thus has the capacity to simulate higher heterogeneity of pore sizes and structure at larger volumes (Fatt, 1956; Blunt et al., 2013; Mahabadi et al., 2016; Piovesan et al., 2019). This approach has been used to investigate the geometry of flow paths in rocks (David, 1993). In addition, it has been used to upscale a wide range of pore-scale phenomena such as viscous drag, capillarity, phase change, and displacement (Blunt, 2017). Flow in porous media strongly relates to the localization due to pore-scale heterogeneity. Localization and preferential flow paths contribute to the difference in intrinsic permeability (Jang et al., 2011). Bernabé and Bruderer (1998) assessed the validity of several permeability models as a function of the variance of the pore size distribution. However, few studies focus on the flow properties in soils considering various pore characteristics, i.e. pore sizes, connectivity, and anisotropy using pore network modeling (Raoof et al., 2011; Raoof and Hassanizadeh, 2012).

This study is an investigation of the flow properties in saturated soils with pores varying in size, connectivity, and anisotropy using pore network modeling. The obtained intrinsic permeability, water pressure distributions, flow patterns, and critical flow paths are analyzed and discussed. The results enhance the fundamental understanding of non-uniform flow induced by the heterogeneity of pore characteristics.

2 Pore network modeling

2.1 Methodology

In pore network modeling, the void space in soils is typically simplified by spherical pore bodies (i.e. pores, hereafter) interconnected by cylindrical pore throats (i.e. throats, hereafter). More sophisticated

geometries of the pores and the throats have also been used to replicate more realistic pore geometry of the soils (Blunt et al., 2013). In this study, all the numerical implementations are performed using OpenPNM, which is an open-source package in Python for pore network simulations (Gostick et al., 2016).

According to the Hagen-Poiseuille equation, the hydraulic conductance of a throat α_t is defined as

$$\alpha_t = \frac{\pi R_t^4}{8\eta \Delta L_t}, \tag{1}$$

where R_t and ΔL_t are the radius and the length of the throat, respectively; η is the viscosity of the fluid.

The flow rate through the throat q_t can be described as

$$q_t = \alpha_t \Delta P_{i\text{-}j}, \tag{2}$$

where $\Delta P_{i\text{-}j}$ is the pressure difference across the throat.

It is assumed that the pores have no flow resistance, so the pressure loss in each pore can be neglected (Wu et al., 2010; Qin and Hassanizadeh, 2015; Gostick et al., 2016). The total flow rate into and out of each pore q_p should satisfy mass conservation:

$$\sum q_p = 0. \tag{3}$$

Combining Eqs. (2) and (3), the pressure at a central pore P_c can be determined as a function of the pressure at all neighboring pores P_i:

$$P_c = \frac{\sum \alpha_{t,i} P_j}{\sum \alpha_{t,i}}. \tag{4}$$

Therefore, the pressure at all the internal pores can be written by Eq. (4), and thus a matrix form can be obtained as

$$\boldsymbol{AX} = \boldsymbol{B}, \tag{5}$$

where $\boldsymbol{A}$ is a matrix composed of throat conductivities; vector $\boldsymbol{X}$ contains the unknown pressures at different pores; vector $\boldsymbol{B}$ captures known boundary pressures.

Based on Eqs. (1)–(5), the pressures at all the pores and the flow rates in all the throats in the network can be calculated with known pore characteristics and fluid properties at given boundary pressures. The intrinsic permeability of the whole network K can be determined as

$$K = \eta \frac{Q_{out}}{\Delta P} \frac{L}{A}, \tag{6}$$

where Q_{out} is the total flux at the outlet of the network; ΔP is the pressure difference across the network domain (i.e. between the inlet and outlet boundaries); L and A are the length and the cross-sectional area of the network domain, respectively.

The accuracy and effectiveness of pore network model simulations for predicting permeability and multiphase flow properties in porous media via extracted pore networks have been experimentally validated (Al-Kharusi and Blunt, 2008; Dong and Blunt, 2009; Blunt et al., 2013; Wang et al., 2015; Bultreys et al., 2016). Admittedly, the simplified pore geometries used in this study will not give accurate estimations of absolute permeability values, but rather qualitative understanding of the correlations between pore characteristics and flow behavior.

2.2 Network calibration and determination

In this study, the pore networks are 3D lattice structures with simple cubic packing as shown in Fig. 1a (Mu et al., 2008; Wu et al., 2010). The coordination number (cn) for characterizing the pore connectivity is assigned as 6, which means one central pore is interconnected with six surrounding throats stretching in lateral and vertical orientations. To optimize the computational cost and efficiency, pore networks with various domain sizes are tested. The networks have cross-sections consisting of 10×10, 20×20, or 50×50 pores and the height of the longitudinal direction (i.e. along with the flow direction) varies from N_f=10, 50, and 100 to 200 pores, where N_f is the number of pores in the flow direction. The imperfectly cubic networks enable us to evaluate the effect of domain size on computed intrinsic permeability from the perspective of both the cross-section and the height. Published data show that most natural sediments exhibit a log-normal distribution in pore size with an average coefficient of variation (i.e.

standard deviation σ over mean value μ) of COV=σ/μ=0.4 with lower and upper bounds of 0.2 and 1.0, respectively (Phadnis and Santamarina, 2011). Even though some of the soils are better described by other distributions (e.g. Weibull distribution), porous media with log-normally distributed pore sizes are widely used in theoretical and numerical models of soils (Kosugi, 1996, 1999; Friedman and Seaton, 1998; Tuli et al., 2001; Dai and Santamarina, 2013; Qin et al., 2016). Here, the pore diameters d_p in the networks are generated to satisfy a truncated log-normal distribution in a range of 0 μm<d_p<30 μm with a mean pore diameter μ_d=10 μm and a standard deviation σ_d=4 μm (note that the pore diameters in all networks used in this study follow truncated distributions with the same lower and upper cutoffs). The magnitude of pore sizes can be found in silt and silty sand (Hwang and Powers, 2003). The center to center distance of neighboring pores is 30 μm. The throat diameter is assumed to be the diameter of the smaller pore connecting at the two ends of the throat to maintain physical consistency (Gostick et al., 2007, 2016). Constant pressures of 206 kPa and 103 kPa are assigned to the pores located at the top and the bottom sides of the networks, respectively, and the other four boundaries are insulated. Steady-state flow is performed to calculate the intrinsic permeability of the networks with different domain sizes. Fig. 1b shows the water pressure distribution results in a 50×50×50 network.

For each tested domain size, 20 random realizations are calculated and their intrinsic permeability results are summarized in Fig. 1c. Ideally, the larger the network size, the less scattered it is in calculated permeability but more computationally expensive. For instance, using a 3.4 GHz processor, it takes ~15 min to compute the intrinsic permeability for a 50×50×50 network, whereas the run time will increase to ~90 min for a 50×50×100 pore network. The results in Fig. 1c suggest that the 50×50×50 network can save computing time while achieving adequate accuracy. Note that one can add boundary pores/throats to serve as the input/output regions (Qin and Hassanizadeh, 2015; Qin et al., 2016), while the impact of added boundary pores/throats on the intrinsic permeability of the 50×50×50 pore network is negligible and thus is not adopted here. Therefore, the following simulations all use 50×50×50 pore networks but with different pore sizes, distributions, connectivity, and anisotropy.

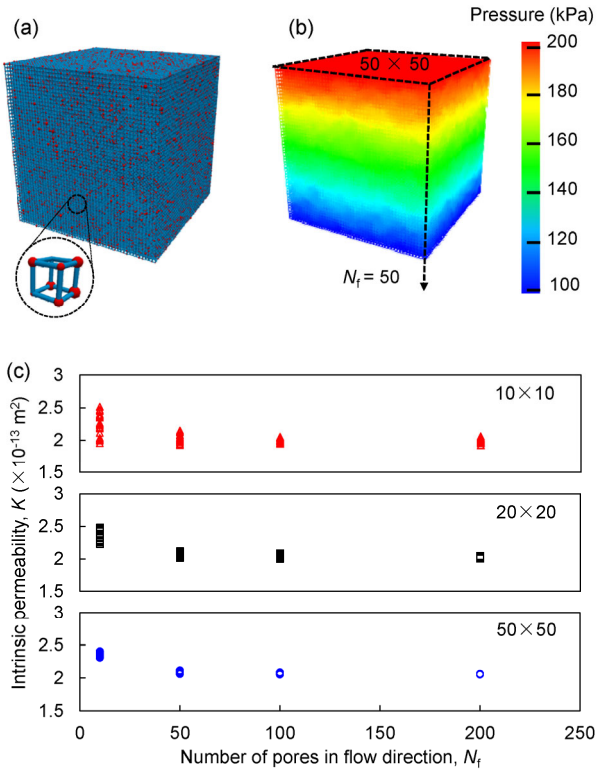

Fig. 1 Influence of domain size on computed intrinsic permeability

(a) An illustrative 3D lattice pore network (i.e. coordination number cn=6) in a cubic domain with 50×50×50 pores. The pore diameters follow a truncated log-normal distribution with mean value μ_d=10 μm and standard deviation σ_d=4 μm. (b) Water pressure distribution within the pore network subjected to 206 kPa pressure at the top and 103 kPa at the bottom with other four boundaries insulated. (c) Computed intrinsic permeability in pore networks with identical pore size distribution, but different cross-sectional areas (i.e. 10×10, 20×20, and 50×50 pores) and lengths (N_f=10, 50, 100, and 200 pores). Each domain size has 20 random realizations

3 Numerical results

3.1 Intrinsic permeability

Fig. 2a shows the change in intrinsic permeability K and porosity Φ in response to the change in the mean pore diameter μ_d. The pore diameters follow a log-normal distribution with a constant σ_d of 4 μm and various μ_d ranging from 4 μm to 20 μm to reach the desired COV range of 0.2–1.0. It can be seen that a

larger μ_d leads to a larger porosity, and thus increases the intrinsic permeability accordingly. As the mean pore diameter increases from 4 μm to 20 μm, the intrinsic permeability can increase by three orders of magnitude. The variation of intrinsic permeability and porosity with different σ_d is shown in Fig. 2b. The pore diameters in the networks follow a log-normal distribution with a constant μ_d of 10 μm. In order to reach the desired COV range of 0.2–1.0, various σ_d in a range of 2–10 μm are assigned in the networks. As σ_d increases, the porosity and intrinsic permeability decrease, which is in agreement with the results of Jang et al. (2011). The development of porosity and intrinsic permeability with the variation of coordination number is shown in Fig. 2c. A log-normal pore diameter distribution (PSD) is assigned in the networks with μ_d=10 μm and σ_d=4 μm (COV=0.4). The pore network with cn=12 is first generated (each throat stretches along the diagonal lines of the central pore), then some throats are randomly removed to create networks with average cn of 4, 6, 8, and 10. The dangling ends and isolated pores induced by the removal of throats are also removed. Fig. 2c shows that both the porosity and permeability increase linearly with increased cn (within the range of investigation, i.e. cn=4–12). Higher pore connectivity provides more flow channels and thus results in higher intrinsic permeability. These results are consistent with the percolation theory that indicates the power law $K \propto (\Phi-\Phi_c)^t$ (Berkowitz and Balberg, 1993). The parameter t is a non-universal exponent, t>2 (Ghanbarian et al., 2014). Φ_c is the critical porosity (i.e. the percolation threshold in terms of porosity), and Φ_c can be replaced by 1.5Φ/cn for 3D pore networks based on bond percolation theory (Sahimi, 1993; Ghanbarian et al., 2015). Thus, we can obtain the power law $K \propto [\Phi(1-1.5/\text{cn})]^t$ which indicates that an increase in Φ or cn can lead to an increase in K. Fig. 2d shows the variation of porosity and intrinsic permeability with different distributions of pore diameters, which all range within 0–30 μm. Among the three different types, the smallest porosity and the smallest intrinsic permeability are found in the network with log-normal distribution of pore sizes. Interestingly, the normal distribution provides the largest porosity but an

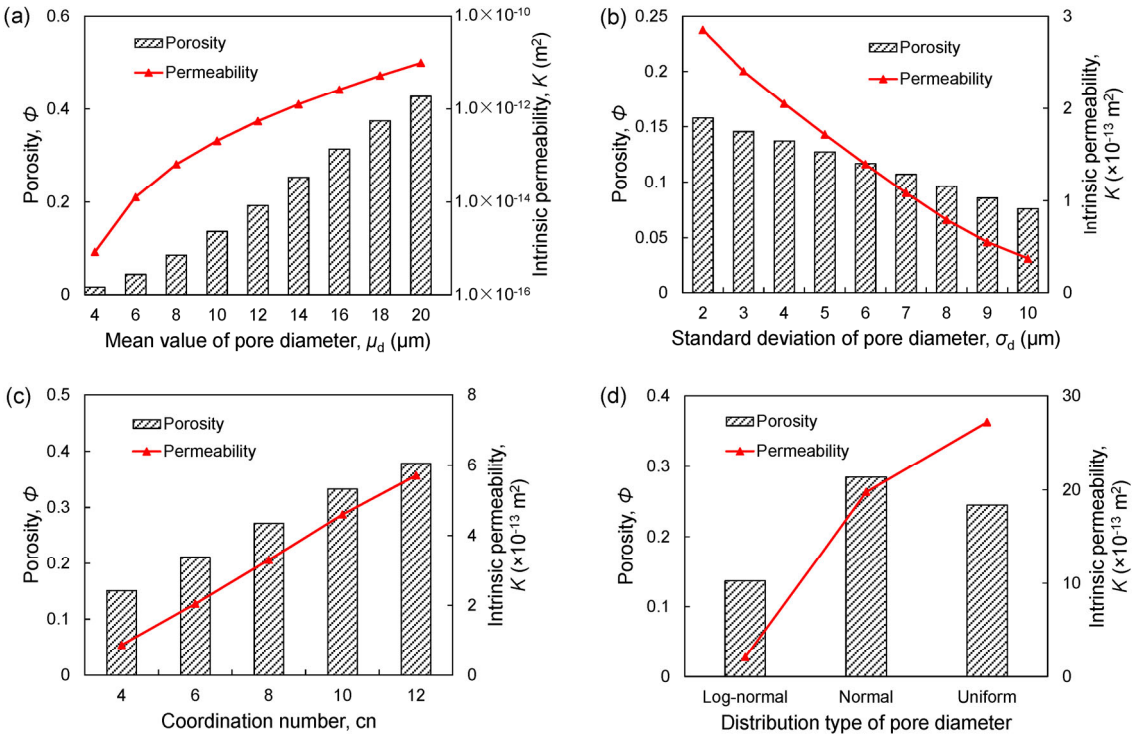

Fig. 2 Intrinsic permeability and porosity affected by various pore characteristics

(a) Mean value of pore diameter; (b) Standard deviation of pore diameter; (c) Coordination number; (d) Distribution type of pore diameter. The cases in Figs. 2a–2c use pore networks with the pore diameters following a truncated log-normal distribution. The pore diameters in all networks are distributed within the identified range of 0–30 μm

intermediate intrinsic permeability. The uniform distribution provides intermediate porosity but the largest intrinsic permeability. More preferential flows will appear in the network with the uniform PSD due to the higher heterogeneity of pore sizes (Fig. 3c), and that helps increase the intrinsic permeability. The flow patterns in the networks will be discussed in the following sections to support the above explanation.

3.2 Water pressure distribution

Figs. 3a–3c show the water pressure distributions within the networks in the above simulations using the ParaView software (Ahrens et al., 2005). Also, each figure presents the PSDs, throat diameter distributions, and corresponding water pressure distributions at the middle section perpendicular to the flow direction. Previous studies indicate that the spatial distributions of pressure and flow are identical for the networks with the same COV of log-normally distributed pore sizes although the overall magnitude may be different (Friedman and Seaton, 1998; Kim and Santamarina, 2015). Therefore, the networks with identical μ_d but various σ_d are selected to investigate the impact of COV on the water pressure distribution. As the COV increases, both the pore and throat diameter distributions become more evidently right-skewed and present a larger broadness as indicated in Fig. 3a. The increased broadness of PSD increases the heterogeneity of the network, resulting in an increasingly non-uniform water pressure field in the network. As the cn increases, although the PSD maintains unchanged, the number of throats of a given diameter shifts to a higher value. The water pressure becomes more uniform with the increase in cn as shown in Fig. 3b. In the network with a higher cn, the water pressure at each pore can be balanced by more throats, and thus can mitigate the pressure localization and produce a more uniform pressure field. Among the networks with uniform, normal, and log-normal PSDs, the uniform and normal PSDs provide the highest and lowest heterogeneity of pore sizes, respectively. Therefore, the pressure field is the most uniform in the network with the normal PSD due to more homogeneous pore diameters and the least uniform in the one with the uniform PSD due to the largest heterogeneity of pore sizes.

3.3 Flow rate distribution

The distributions of flow rates in throats at both the middle section and the outlet boundary of the networks for the above simulations are obtained. For each cross-section, we add up the flow rate in each throat in descending order of magnitude, and then we can obtain the relationship between the number of throats N and the accumulated flux Q carried by these throats. The results are presented in a normalized form, i.e. the number of throats N is normalized by the total throat number N_t, and the flux Q is normalized by the total flux Q_t. Fig. 4a (p.968) summarizes the relationship between Q/Q_t and N/N_t at the middle section and the outlet boundary for the network with COV=0.4 (μ_d=10 μm) and cn=6. It can be found that the same number of throats carry more fluid at the outlet boundary compared with the middle section, indicating a higher degree of non-uniform flow rate distribution. As the water pressure at each pore is identical at the outlet boundary, the flow rate is dominantly controlled by the pore sizes. Therefore, it can be speculated that non-uniform water pressure in the middle section (Fig. 3a) contributes to mitigating the non-uniform flow induced by the heterogeneity of pore sizes. On the basis that the relationship between Q/Q_t and N/N_t at the middle section has a similar shape to that at the outlet boundary, the relationship for the latter cross-section is not plotted in Figs. 4b–4d to avoid redundancy. Fig. 4b shows that soils with pores with a larger COV lead to a more heterogeneous flow rate distribution in the middle section and at the outlet boundary. Fig. 3a illustrates that the throat diameters become more evidently right-skewed as the COV increases, meaning more relatively large throats appear in the network. These relatively large throats contribute to the non-uniform flow because they have the capacity to carry more fluid. To carry 50% of the total flux, the number of the corresponding throats decreases with increasing COV values as indicated in the inset of Fig. 4b. For the network with mono-sized pores (i.e. COV=0), 50% of the throats can carry 50% of the total flux, implying a uniform flow regime. As COV increases to 1.0, as few as 7% and 5% of total throats are responsible for 50% of the total flux in the middle section and at the outlet boundary, respectively. Fig. 4c shows the effect of cn on the relationship

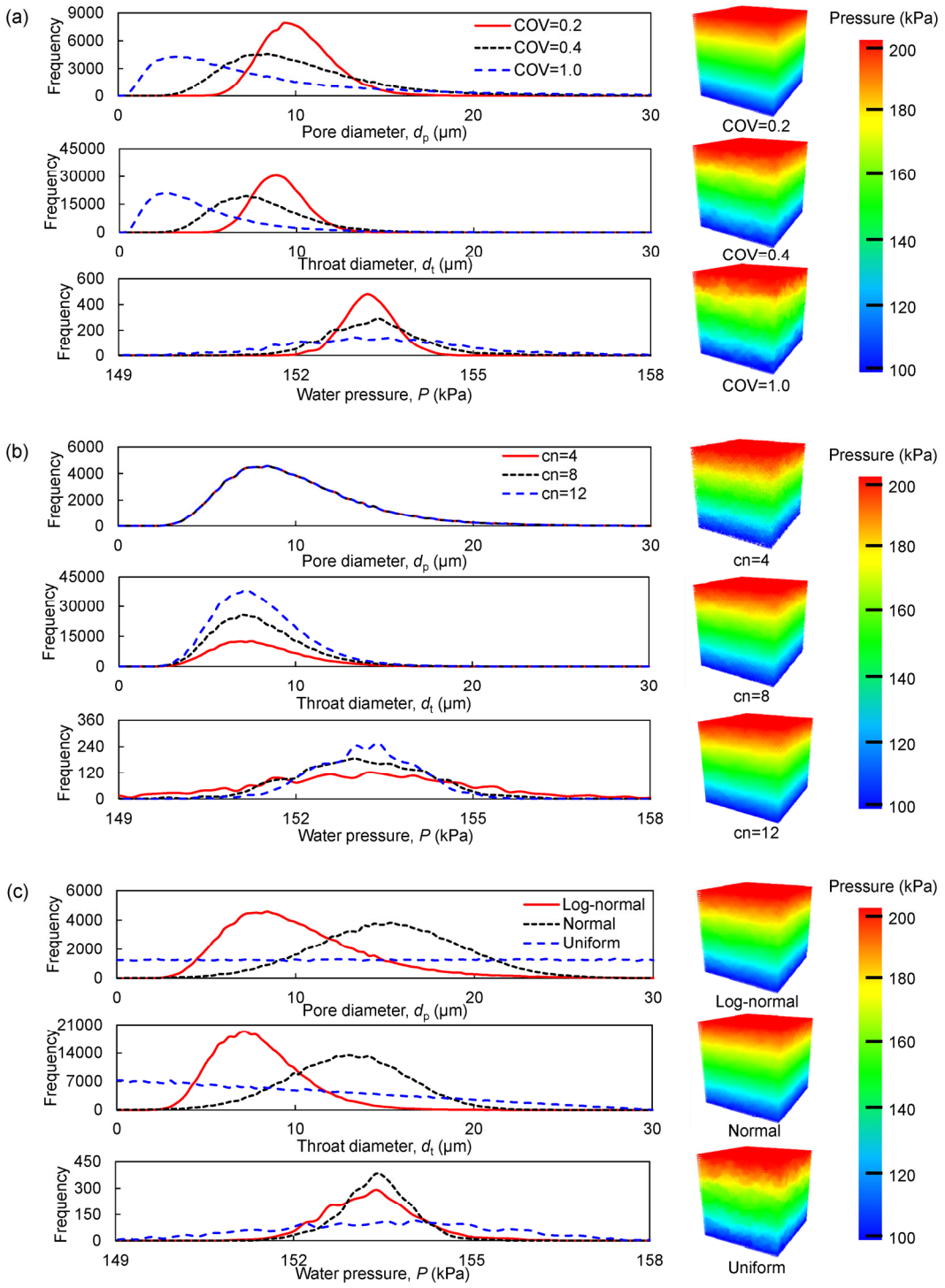

Fig. 3 Water pressure distribution affected by various pore characteristics

(a) Log-normal PSDs with three different COVs (all cases are with identical μ_d=10 μm and cn=6; a larger COV results in a more non-uniform water pressure field). (b) Log-normal PSDs with three different cn (all cases are with identical μ_d=10 μm and σ_d= 4 μm; a smaller cn results in a more non-uniform water pressure field). (c) Log-normal, normal, and uniform PSDs (the pressure field is the most uniform in the network with the normal PSD and the least uniform in the one with the uniform PSD). In each figure, PSDs are shown at the top, throat diameter distributions are shown in the middle, water pressure distributions at the middle sections perpendicular to the flow direction are shown at the bottom, and water pressure distributions within the networks are shown on the right

between Q/Q_t and N/N_t. At the middle section, the same number of throats carry slightly less fluid for a lower cn in the flux range of 0%–80%. As previously mentioned, the middle section in the network with cn=4 has the most non-uniform water pressure distribution and thus leads to more pronounced mitigation of the non-uniform flow regime than a higher cn. As shown in the inset, the insignificant impact of cn on the flow rate distribution is found at the outlet boundary due to the same PSD and identical water pressure of 103 kPa applied at this cross-section for various cn. Among the three distribution types, the uniform PSD presents the most non-uniform flow rates and the normal PSD presents the least non-uniform flow rates, as shown in Fig. 4d.

3.4 Flow intensity and pattern

The relationships between Q/Q_t and N/N_t within the whole networks are obtained. The flow patterns in the above-mentioned simulations are visualized using the ParaView software, as shown in Fig. 5. For a better illustration, not all throats in the network are shown. Throats become visible starting from the one with the highest flow rate and then the next highest progressively until these visible throats can carry 10% of the total network flux. The magnitude of flow rate in each throat is indicated by different colors, and the mean diameter of the visible throats are shown below the cubes in Fig. 5. As expected, less throats are needed to carry the same fraction of the total flux as

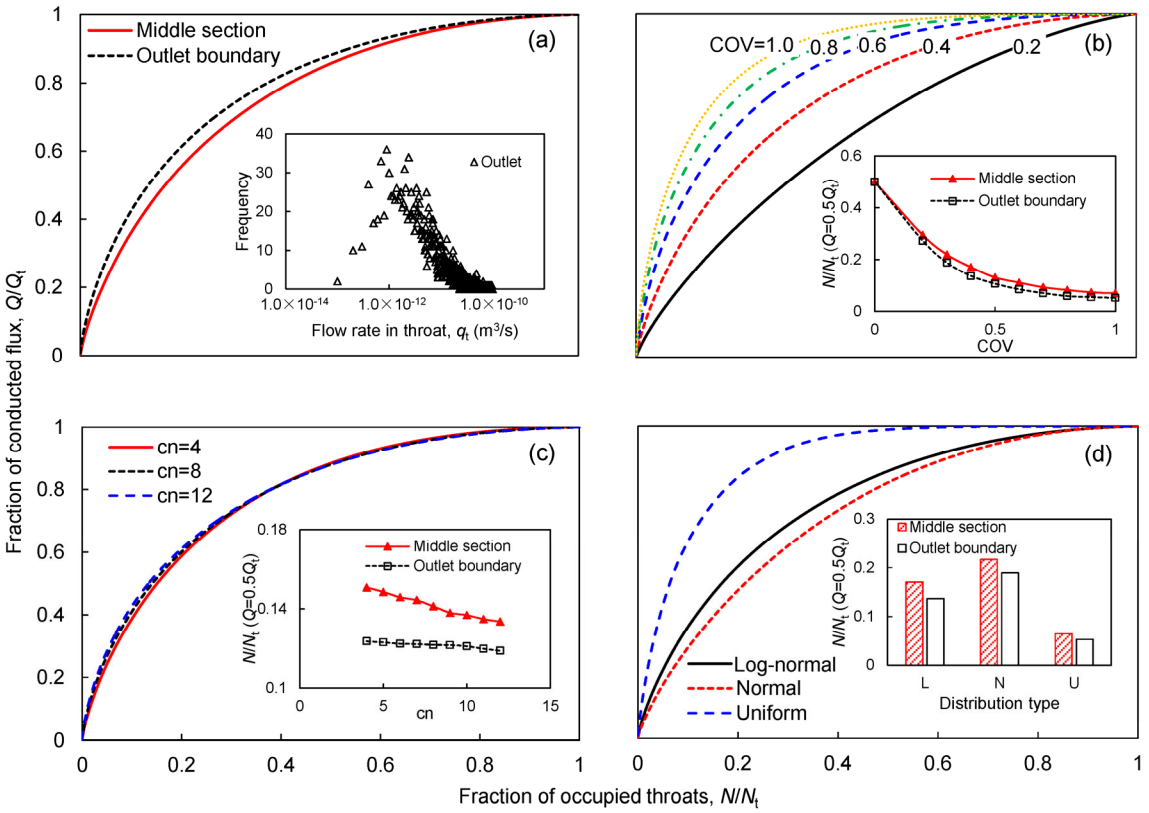

Fig. 4 Flow rates in throats at the middle section and the outlet boundary

(a) Relationship between the number of throats N (normalized by the total throat number N_t) and their conducted flux Q (normalized by the total flux Q_t) at the middle section and outlet boundary. The inset shows the distribution of flow rates in throats at the outlet boundary. The network consisted of log-normally distributed pores with μ_d=10 μm, σ_d=4 μm, and cn=6. (b) Impacts of COV on the flow rates in throats. The inset shows the variation of fraction of throats needed to carry 50% of total flux with the increase in COV. (c) Impacts of cn on the flow rates in throats. The inset shows the variation of fraction of throats needed to carry 50% of total flux with the increase in cn. (d) Impacts of distribution type of pore diameters on the flow rates in throats. The inset shows the fraction of throats needed to carry 50% of total flux for log-normal (L), normal (N), and uniform (U) PSDs

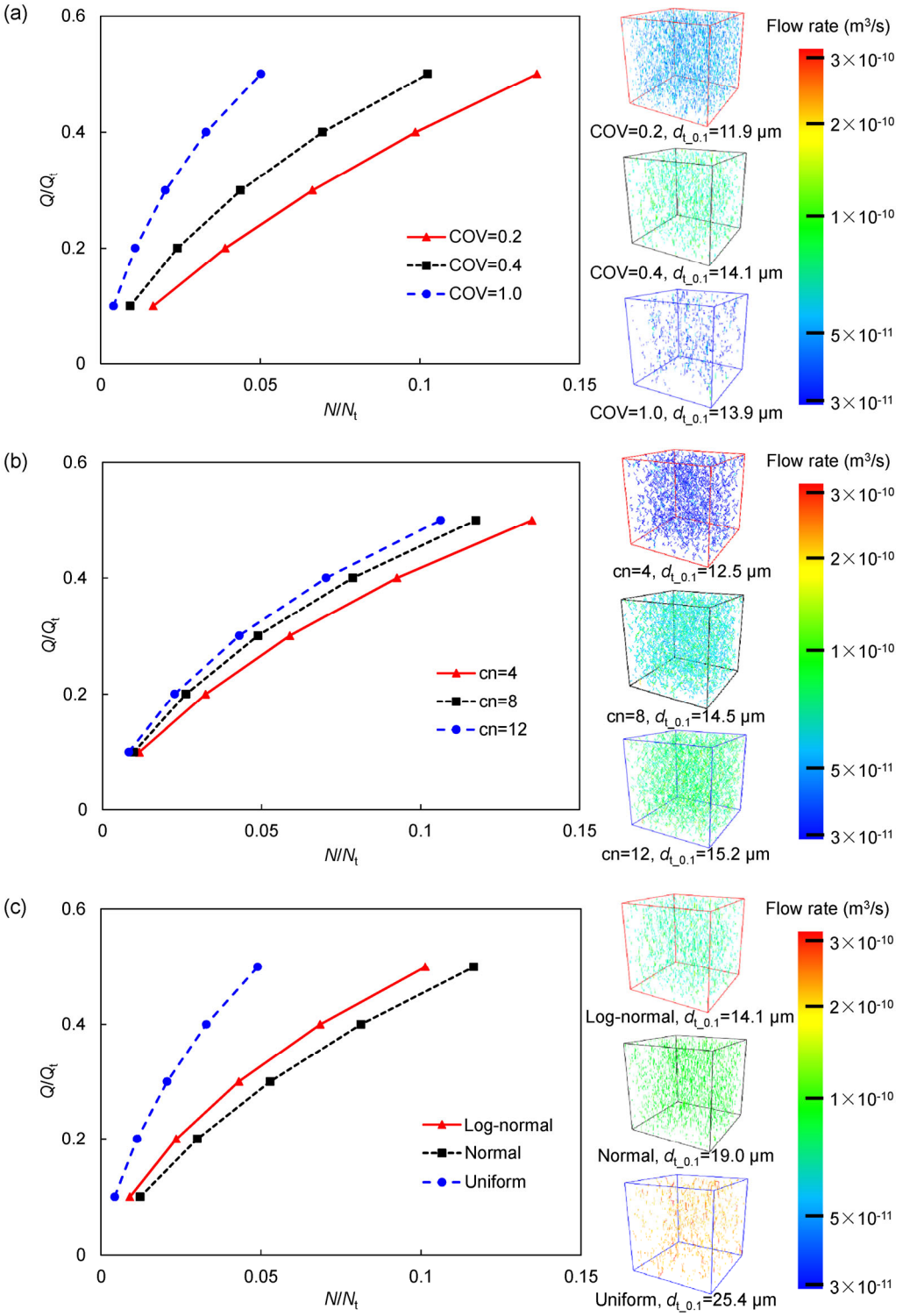

Fig. 5 Flow intensity and pattern affected by various pore characteristics

(a) Flow in three pore networks with different COVs; (b) Flow in three pore networks with different cn values; (c) Flow in three pore networks with three different PSDs of log-normal, normal, and uniform distributions. In each figure, the required fraction of throats N/N_t to carry the corresponding fraction of the domain flux Q/Q_t (10%–50%) is shown on the left, and the flows in these cubes are shown on the right. For better visualization, only throats with high flow rates up to 10% of the total flux are shown. For interpretation of the references to color in this figure, the reader is referred to the web version of this article

COV increases as shown in Fig. 5a, implying a more localized and heterogeneous flow field. This trend can also be clearly recognized from the displayed flow regime in Fig. 5a. The PSD curve becomes more evidently right-skewed for a larger COV as shown in Fig. 3a, meaning the appearance of more relatively large pores. However, a smaller mean diameter of the visible throats ($d_{t\_0.1}$) is found for the network with COV=1.0 compared with that with COV=0.4. This is related to the more non-uniform water pressure distribution that causes some small throats to carry more fluid. Fig. 5b shows that a higher cn can slightly increase the chance of a non-uniform flow field, due to a higher possibility for fluid at each pore to access large throats. For instance, the mean diameter of the visible throats $d_{t\_0.1}$ increases from 12.5 μm to 15.2 μm as cn increases from 4 to 12. Further, the increase in $d_{t\_0.1}$ induces a higher magnitude of the flow rates in the displayed throats as the flow rate in each throat correlates with $d_{t\_0.1}$. Compared with the normal and log-normal PSDs, the uniform distribution has a broader distribution range of pore sizes, i.e. a higher COV, leading to the most evident non-uniform flow field (Fig. 5c). For instance, to transport 50% of the total flux, it requires approximately 12% of the throats in the network with normal PSD, but only 5% of the throats in a network with uniform PSD. In addition, the uniform PSD presents the highest magnitude of the flow rates, due to having the largest $d_{t\_0.1}$ among the three distribution types.

4 Analyses and discussion

4.1 Critical flow path

The heterogeneity of pore sizes can induce critical flow paths in soils. The critical path analysis enables us to characterize critical flow paths in terms of critical conductance or critical length scales. These valuable parameters allow us to assess the transport processes and predict the conductivity of rocks and soils (Ambegaokar et al., 1971; Hunt et al., 2014). Similarly, critical flow paths can be evaluated by the percolation path, which is a single continuous path that carries the largest amount of flux compared with all other flow paths in the network (note that the percolation path is also defined as the "most efficient flow path" in (David, 1993)). Experimental evidence demonstrates that the percolation path controls the overall conductivity of the network (Agrawal et al., 1991), and thus knowing its properties is valuable. Although 3D networks can provide more accurate results than 2D networks, the flow paths in 3D networks will not be easy to display and evaluate. Therefore, for a better illustration, the flow paths at the moment of percolation in 2D square networks (50×50 pores, cn=4) are shown (Fig. 6a). The percolation path is obtained as follows: we firstly map the throats that carry more than an arbitrary threshold value of flow rate, and then we increase/decrease the threshold value progressively until a continuous path from the top to the bottom boundaries of the network is formed. The tortuosity is defined as the ratio between the total number of throats in the backbone of the percolation path and the number of throats in a straight streamline parallel to the flow direction (David, 1993; Jang et al., 2011). Note that the pressure gradient is in the vertical direction without considering the gravitational effect in all simulated networks, and the magnitude of the flow rate in each throat is reflected by the throat diameter in Fig. 6a. In a perfectly homogeneous network (i.e. COV=0), no flow takes place in the horizontal throats (perpendicular to the pressure gradient), and each vertical streamline (parallel to the pressure gradient) is an individual percolation path with tortuosity of 1.00. The fraction of total flux that each percolation path carries Q_{pp}/Q_t is identical and can be determined as 1/50=2.0% (50 columns in the network). In the network with COV=0.2, some horizontal throats are involved in contributing to the percolation path and the tortuosity becomes ~1.10, but the vertical flow still dominates. As the flow becomes heterogeneous, not all the visible throats constitute the percolation path as shown in Fig. 6a. The amount of flux that the percolation path carries can be approximately determined by multiplying the flux carried by all the visible throats by a number factor, which is defined as the number of the throats in the percolation path over the total number of the visible throats. Based on this process, we obtain Q_{pp}/Q_t=2.3% when COV=0.2, slightly larger than that in the homogeneous network. With the increase in COV, the flow becomes more and more tortuous. The increase in the number of horizontal throats involved

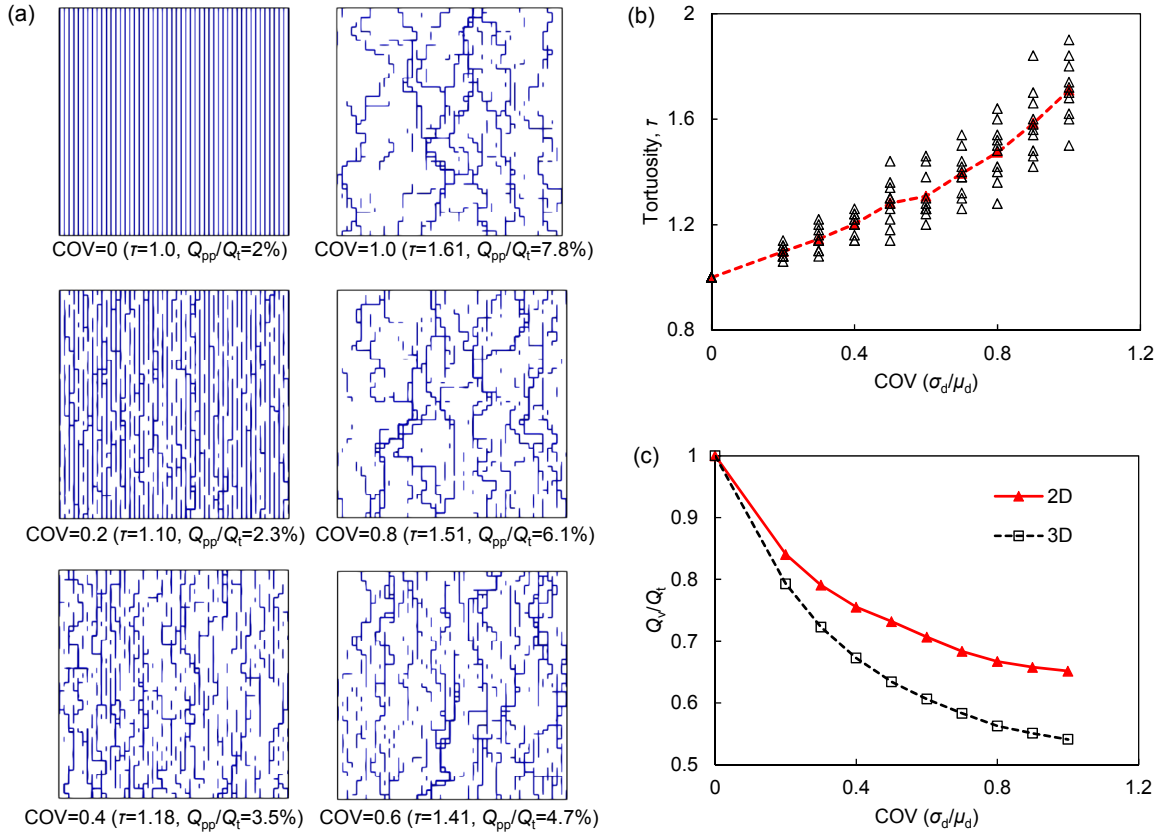

Fig. 6 Critical flow paths affected by the COV of pore sizes

(a) Flow paths at the moment of percolation in 2D square pore networks with various COV values. The magnitude of the flow rate in each throat is reflected by the throat diameter. (b) Tortuosity of the percolation path increasing with COV. (c) Flux carried by vertical throats Q_v (normalized by the total domain flux Q_t) decreasing with increasing COV

in forming the percolation path increases the tortuosity to ~1.71 at COV=1.0 (Fig. 6b, each case has 10 realizations). In this situation, the percolation path carries 7.8% of the total flux, which is more than three times higher than that in the homogeneous network, indicating the appearance of preferential flows in the network. Fig. 6c shows the ratio of the flux carried by all vertical throats over the total flux (Q_v/Q_t) in networks (both 2D and 3D) with different COV values. As the COV increases, horizontal throats begin to carry more flux. At COV=1.0, the horizontal throats conduct approximately 35% and 45% of total flux for 2D and 3D networks, respectively. It should be noted that 3D networks provide lower Q_v/Q_t at the same COV compared with 2D networks. This is reasonable because the central pores have 4 and 2 interconnected horizontal throats in the 3D and 2D models, respectively, and hence more optional flow paths along the horizontal direction appear for a 3D network. Thus, it is expected that a larger tortuosity of the percolation path will appear in a 3D model than in a 2D model with the same COV.

Fig. 7a illustrates the flow paths at the moment of percolation in 2D square networks with log-normal, normal, and uniform PSDs. In networks with log-normal and normal PSDs, considerable discontinuous paths can be found in addition to the percolation path. The percolation paths carry 3.5% and 2.6% of the total flow for log-normal and normal distributions, respectively. The normal distribution presents a close tortuosity (i.e. 1.16) to the log-normal distribution (i.e. 1.18). Vertical throats conduct more than (or close to) 70% of total flux for both 2D and 3D models in the two cases as shown in Fig. 7b. However, this is not the case in the network with uniform PSD where the percolation path performs as a dominant path that can

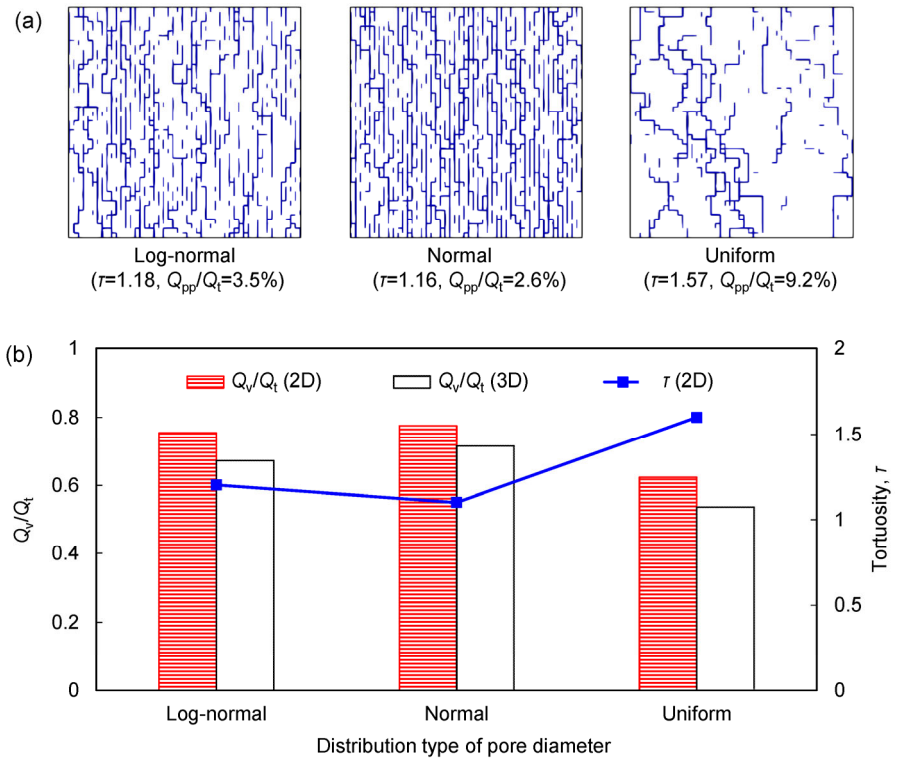

Fig. 7 Critical flow paths affected by the distribution type of pore diameters

(a) Flow paths at the moment of percolation in 2D square pore networks with log-normal, normal, and uniform PSDs. The magnitude of the flow rate in each throat is reflected by the throat diameter. (b) Tortuosity and flux carried by vertical throats Q_v (normalized by the total domain flux Q_t) for the three different distribution types

carry as much as 9.2% of the total flux. The dominant flow plays an important role in increasing the intrinsic permeability of soils. This can explain why the uniform distribution has a lower porosity but a greater intrinsic permeability compared with the normal distribution (Fig. 2d). Due to the higher degree of heterogeneity in the flow field, the tortuosity, in this case, is also significantly higher: τ=1.57. The horizontal throats conduct approximately half the total flux as the horizontal throats do for the 3D networks.

4.2 Effects of anisotropy

Sedimentation and segregation can cause stratification and anisotropy in natural soils. Flows in anisotropic soils with different horizontal to vertical throat diameter ratios μ_{dh}/μ_{dv} are investigated using 2D and 3D networks. These networks are constructed initially using log-normally distributed pores with COV=0.4 and cn=4 (2D) or cn=6 (3D), and then a throat size reduction factor k_h is applied to all the horizontal throats $\mu_{dh}=k_h\mu_d$, to render anisotropic networks with $\mu_{dh}/\mu_{dv}<1$. The reduction factor k_v is applied to all the vertical throats $\mu_{dv}=k_v\mu_d$ to generate $\mu_{dh}/\mu_{dv}>1$. Fig. 8a shows the obtained flow paths at the moment of percolation in the 2D networks with μ_{dh}/μ_{dv} varying from 1/5 to 5/1. The flow becomes more tortuous and the percolation path carries a greater fraction of the total flux as μ_{dh}/μ_{dv} increases. However, no clear dominant flow path appears as indicated by Fig. 8a, and the percolation path can carry 3.0%–5.8% of total flux. As the μ_{dh}/μ_{dv} ratio increases, more horizontal throats will contribute to the percolation path, resulting in an increase in the tortuosity of the percolation path. The tortuosity increases from 1.00 when μ_{dh}/μ_{dv}=0.2 (i.e. vertical throats are four times larger than horizontal ones) to ~2.27 when μ_{dh}/μ_{dv}=5 (i.e. horizontal throats are four times larger than vertical ones). As shown in Fig. 8b, a significant increase in tortuosity takes place when $\mu_{dh}/\mu_{dv}>1$, indicating the reduction in vertical throats rather than in horizontal throats has more effect on tortuosity.

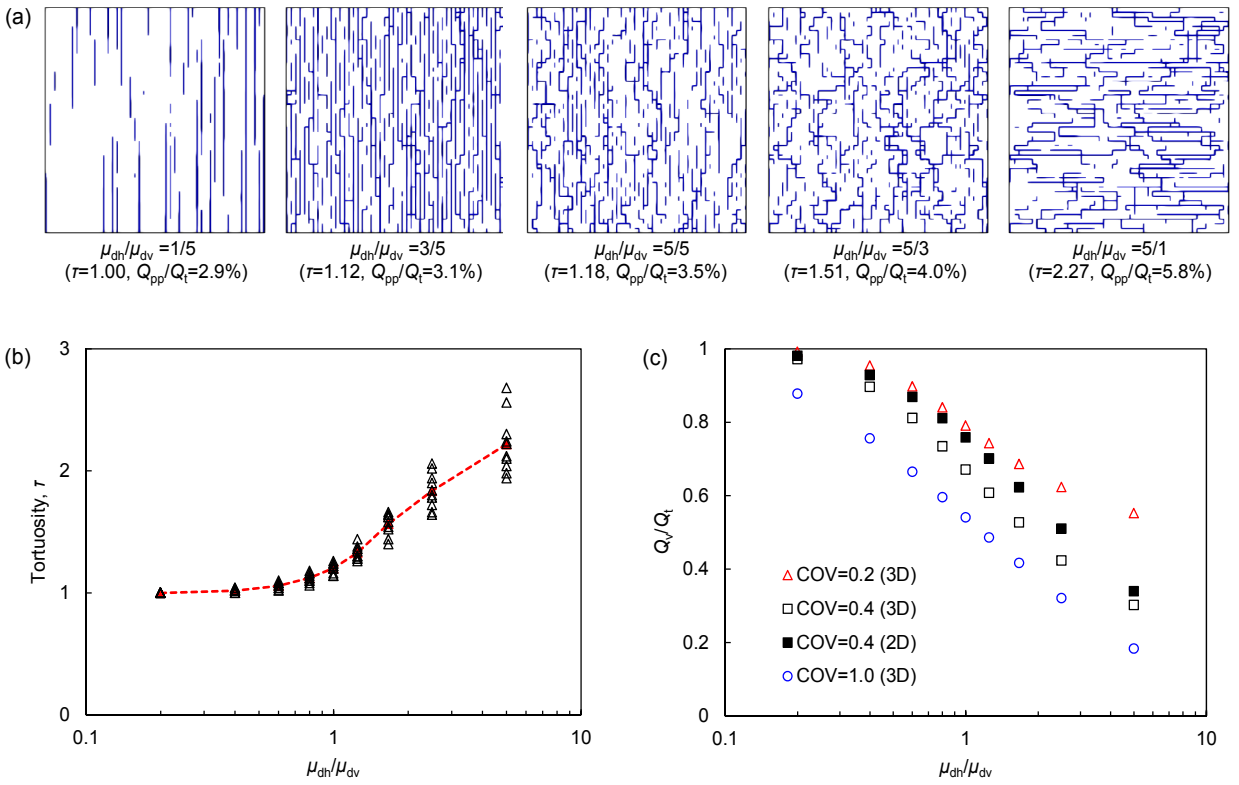

Fig. 8 Impacts of throat size anisotropy on critical flow paths

(a) Flow paths at the moment of percolation in 2D square pore networks with various horizontal to vertical throat diameter ratios μ_{dh}/μ_{dv}. The magnitude of the flow rate in each throat is reflected by the throat diameter. (b) Tortuosity of the percolation path increasing with the increase in μ_{dh}/μ_{dv} ratio (2D). (c) Flux carried by vertical throats Q_v (normalized by the total domain flux Q_t) decreasing with the increase in μ_{dh}/μ_{dv} ratio

Results in Fig. 8c show that vertical throats carry most of the total flux (i.e. $Q_v/Q_t \approx 1$) when vertical throats are approximately four times larger than the horizontal ones (i.e. $\mu_{dh}/\mu_{dv} \approx 0.2$). With the increase in the μ_{dh}/μ_{dv} ratio, the flux in the vertical throats contributes less to the total flux. At the point when the horizontal throats are four times larger than the vertical ones ($\mu_{dh}/\mu_{dv}=5$), the horizontal flux dominates the total flow in the 2D network with COV=0.4 as the horizontal throats carry ~70% of the total flux. Additionally, compared with the 2D networks with COV=0.4, the horizontal flow is more pronounced in 3D networks, highlighting that increased pore connectivity can help enhance anisotropy-induced non-uniform flow. In soils with more homogeneous pore sizes, for instance, the case of the 3D networks with COV=0.2, the vertical throats carry nearly 55% of the total flow even when the horizontal throats are four times larger. On the contrary, Q_v/Q_t can decrease to less than 20% in a more heterogeneous network (e.g. COV=1.0). This result highlights the importance of throat sizes and orientation with respect to the anisotropy of flow in soils.

The effect of throat size anisotropy on the intrinsic permeability in soils is also investigated. Fig. 9a shows the variation of K_h/K_v with increasing μ_{dh}/μ_{dv}, in which K_h and K_v are the horizontal and vertical intrinsic permeability of the anisotropic network, respectively. It can be found from Fig. 9a that the intrinsic permeability is smaller in the direction with a smaller throat diameter. Fig. 9a also illustrates that K_h/K_v increases as μ_{dh}/μ_{dv} increases, and the relation of K_h/K_v and μ_{dh}/μ_{dv} presents a nearly straight line in logarithmic coordinates. The influence of throat size anisotropy on the permeability ratio, K_h/K_v, for the network with a larger COV is less significant. Similarly, owing to the higher pore size variability, K_h/K_v in the network with the uniform PSD is less

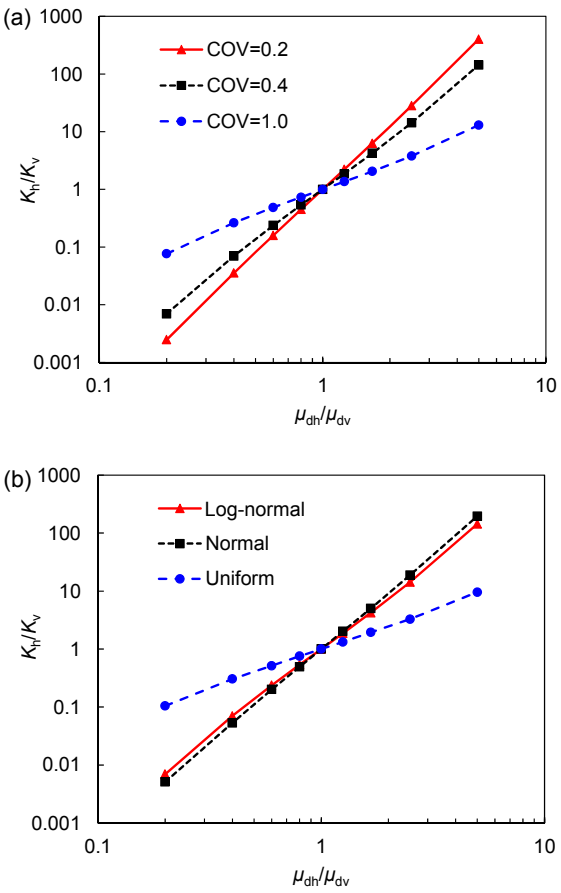

Fig. 9 Impacts of throat size anisotropy on intrinsic permeability

(a) Ratio of horizontal permeability over vertical permeability K_h/K_v versus horizontal to vertical throat diameter ratio μ_{dh}/μ_{dv} in networks with three different COVs of pore diameters; (b) K_h/K_v versus μ_{dh}/μ_{dv} in networks with three different distribution types of pore diameters

sensitive to μ_{dh}/μ_{dv} compared with those in networks with the log-normally and normally distributed pore sizes as shown in Fig. 9b.

5 Conclusions

This study investigates the influence of pore characteristics on flow properties in soils. Pore-network modeling is used to obtain the intrinsic permeability, water pressure distributions, flow patterns, and critical flow paths in soils possessing various pore sizes, connectivity, and anisotropy. Networks with 50×50×50 spherical pores interconnected by cylindrical throats are constructed to conduct the simulations. Based on the numerical results, the following conclusions can be drawn:

1. The porosity and the intrinsic permeability in soils increase with increasing mean pore diameter μ_d, decreasing standard deviation σ_d, and linearly with increasing coordination number cn. Among the three types of log-normal, normal, and uniform PSDs with the same range of pore diameters, both the smallest porosity and the smallest intrinsic permeability appear in a log-normal distribution. The normal distribution presents the largest porosity but intermediate intrinsic permeability. The uniform distribution presents intermediate porosity but the largest intrinsic permeability resulted from preferential flows induced by a high degree of heterogeneity in pore sizes.

2. Non-uniform distributions of water pressure and flow rate are more likely to occur in porous media with a larger COV. With the increase of COV, fewer throats are needed to transport half the total flux in the middle section and at the outlet boundary of the network. In the network with a higher coordination number, the water pressure at each pore can be balanced by more throats. This mitigates the pressure localization and produces a more uniform water pressure field but slightly increases the chance of non-uniform flow rate field. Compared with the log-normal and the normal PSDs, the uniform distribution leads to the most non-uniform water pressure and flow rate field within the network. As few as 5% of total throats can carry 50% of the total network flux.

3. With the increase in COV, a larger number of horizontal throats are involved in contributing to the percolation path, and the flow becomes more tortuous. The tortuosity of the percolation path increases from 1.00 at COV=0 to ~1.71 at COV=1.0. The fraction of flux that the percolation path carries in soils with high pore size variability (7.8% at COV=1.0) can exceed three times that in homogeneous media (2.0%), indicating the appearance of preferential flows in the network. The uniform PSD induces more pronounced preferential flows and the percolation path performs as a dominant path that can carry as much as 9.2% of the total flux. Horizontal throats begin to carry more flux in porous media with higher heterogeneity of pore sizes.

4. As the diameter of the horizontal throats increases with respect to the vertical ones (i.e. increasing μ_{dh}/μ_{dv}), more horizontal throats constitute the percolation path, resulting in an increase in flow tortuosity. The percolation path can carry 3.0%–5.8% of the total flux in a μ_{dh}/μ_{dv} range of 1/5–5/1. The increase in μ_{dh}/μ_{dv} increases the fraction of the total flux carried by horizontal throats, and this effect can be amplified in soils with a higher COV. The permeability anisotropy ratio K_h/K_v increases linearly with the ratio of the horizontal and the vertical throat sizes μ_{dh}/μ_{dv} in logarithmic coordinates.

The results obtained from this study are based on simulations of steady-state flow. Future simulations to investigate the effects of pore characteristics on flow properties in unsaturated soils (e.g. water retention curve and relative permeability) will have great significance. How pore characteristics affect mass transfer (e.g. gas diffusion and solute transport in soils) is also of interest and has significance for further research.

Contributors

Liang-tong ZHAN and Sheng DAI designed the research. Guang-yao LI performed the simulations, processed the corresponding data, and wrote the first draft of the manuscript. Sheng DAI helped to organize and revise the manuscript. Liang-tong ZHAN and Yun-min CHEN revised and edited the final version.

Conflict of interest

Guang-yao LI, Sheng DAI, Liang-tong ZHAN, and Yun-min CHEN declare that they have no conflict of interest.

References

Agrawal DL, Cook NGW, Myer LR, 1991. The effect of percolating structures on the petrophysical properties of Berea sandstone. Proceedings of the 32nd U.S. Symposium on Rock Mechanics, p.345-354.

Ahrens J, Geveci B, Law C, 2005. ParaView: an end-user tool for large-data visualization. *In*: Hansen CD, Johnson CR (Eds.), Visualization Handbook. Elsevier, Amsterdam, the Netherlands, p.1-17.

Al-Kharusi AS, Blunt MJ, 2008. Multiphase flow predictions from carbonate pore space images using extracted network models. *Water Resources Research*, 44(6):W06S01. https://doi.org/10.1029/2006WR005695

Allaire SE, Roulier S, Cessna AJ, 2009. Quantifying preferential flow in soils: a review of different techniques. *Journal of Hydrology*, 378(1-2):179-204. https://doi.org/10.1016/j.jhydrol.2009.08.013

Allaire-Leung SE, Gupta SC, Moncrief JF, 2000. Water and solute movement in soil as influenced by macropore characteristics: 1. Macropore continuity. *Journal of Contaminant Hydrology*, 41(3-4):283-301. https://doi.org/10.1016/S0169-7722(99)00079-0

Ambegaokar V, Halperin BI, Langer JS, 1971. Hopping conductivity in disordered systems. *Physical Review B*, 4(8):2612-2620. https://doi.org/10.1103/PhysRevB.4.2612

Andreini MS, Steenhuis TS, 1990. Preferential paths of flow under conventional and conservation tillage. *Geoderma*, 46(1-3):85-102. https://doi.org/10.1016/0016-7061(90)90009-X

Berkowitz B, Balberg I, 1993. Percolation theory and its application to groundwater hydrology. *Water Resources Research*, 29(4):775-794. https://doi.org/10.1029/92WR02707

Bernabé Y, Bruderer C, 1998. Effect of the variance of pore size distribution on the transport properties of heterogeneous networks. *Journal of Geophysical Research: Solid Earth*, 103(B1):513-525. https://doi.org/10.1029/97JB02486

Bianchi M, Zheng CM, Tick GR, et al., 2011. Investigation of small-scale preferential flow with a forced-gradient tracer test. *Groundwater*, 49(4):503-514. https://doi.org/10.1111/j.1745-6584.2010.00746.x

Blunt MJ, 2017. Multiphase Flow in Permeable Media: a Pore-scale Perspective. Cambridge University Press, Cambridge, UK, p.56-69.

Blunt MJ, Bijeljic B, Dong H, et al., 2013. Pore-scale imaging and modelling. *Advances in Water Resources*, 51:197-216. https://doi.org/10.1016/j.advwatres.2012.03.003

Bultreys T, van Hoorebeke L, Cnudde V, 2015. Multi-scale, micro-computed tomography-based pore network models to simulate drainage in heterogeneous rocks. *Advances in Water Resources*, 78:36-49. https://doi.org/10.1016/j.advwatres.2015.02.003

Bultreys T, de Boever W, Cnudde V, 2016. Imaging and image-based fluid transport modeling at the pore scale in geological materials: a practical introduction to the current state-of-the-art. *Earth-Science Reviews*, 155:93-128. https://doi.org/10.1016/j.earscirev.2016.02.001

Bultreys T, Lin QY, Gao Y, et al., 2018. Validation of model predictions of pore-scale fluid distributions during two-phase flow. *Physical Review E*, 97(5):053104. https://doi.org/10.1103/PhysRevE.97.053104

Dai S, Santamarina JC, 2013. Water retention curve for hydrate-bearing sediments. *Geophysical Research Letters*, 40(21):5637-5641. https://doi.org/10.1002/2013GL057884

David C, 1993. Geometry of flow paths for fluid transport in rocks. *Journal of Geophysical Research: Solid Earth*, 98(B7):12267-12278.

https://doi.org/10.1029/93JB00522

Dong H, Blunt MJ, 2009. Pore-network extraction from micro-computerized-tomography images. *Physical Review E*, 80(3):036307. https://doi.org/10.1103/PhysRevE.80.036307

Fatt I, 1956. The network model of porous media. *Petroleum Transactions*, 207:144-181.

Flury M, Flühler H, 1994. Brilliant blue FCF as a dye tracer for solute transport studies—a toxicological overview. *Journal of Environmental Quality*, 23(5):1108-1112. https://doi.org/10.2134/jeq1994.00472425002300050037x

Friedman SP, Seaton NA, 1998. Critical path analysis of the relationship between permeability and electrical conductivity of three-dimensional pore networks. *Water Resources Research*, 34(7):1703-1710. https://doi.org/10.1029/98WR00939

Gerke HH, 2006. Preferential flow descriptions for structured soils. *Journal of Plant Nutrition and Soil Science*, 169(3): 382-400. https://doi.org/10.1002/jpln.200521955

Gerke HH, van Genuchten MT, 1996. Macroscopic representation of structural geometry for simulating water and solute movement in dual-porosity media. *Advances in Water Resources*, 19(6):343-357. https://doi.org/10.1016/0309-1708(96)00012-7

Ghanbarian B, Hunt AG, Ewing RP, et al., 2014. Theoretical relationship between saturated hydraulic conductivity and air permeability under dry conditions: continuum percolation theory. *Vadose Zone Journal*, 13(8). https://doi.org/10.2136/vzj2014.03.0029

Ghanbarian B, Daigle H, Hunt AG, et al., 2015. Gas and solute diffusion in partially saturated porous media: percolation theory and effective medium approximation compared with lattice Boltzmann simulations. *Journal of Geophysical Research: Solid Earth*, 120(1):182-190. https://doi.org/10.1002/2014JB011645

Ghodrati M, Chendorain M, Chang YJ, 1999. Characterization of macropore flow mechanisms in soil by means of a split macropore column. *Soil Science Society of America Journal*, 63(5):1093-1101. https://doi.org/10.2136/sssaj1999.6351093x

Gostick J, Ioannidis M, Fowler M, et al., 2007. Pore network modeling of fibrous gas diffusion layers for polymer electrolyte membrane fuel cells. *Journal of Power Sources*, 173(1):277-290. https://doi.org/10.1016/j.jpowsour.2007.04.059

Gostick J, Aghighi M, Hinebaugh J, et al., 2016. OpenPNM: a pore network modeling package. *Computing in Science & Engineering*, 18(4):60-74. https://doi.org/10.1109/MCSE.2016.49

Hirashima H, Yamaguchi S, Katsushima T, 2014. A multi-dimensional water transport model to reproduce preferential flow in the snowpack. *Cold Regions Science and Technology*, 108:80-90. https://doi.org/10.1016/j.coldregions.2014.09.004

Hunt A, Ghanbarian B, Saville K, 2013. Unsaturated hydraulic conductivity modeling for porous media with two fractal regimes. *Geoderma*, 207-208:268-278. https://doi.org/10.1016/j.geoderma.2013.05.023

Hunt A, Ewing R, Ghanbarian B, 2014. Percolation Theory for Flow in Porous Media, 3rd Edition. Springer, New York, USA, p.46-55.

Hwang SI, Powers SE, 2003. Using particle-size distribution models to estimate soil hydraulic properties. *Soil Science Society of America Journal*, 67(4):1103-1112. https://doi.org/10.2136/sssaj2003.1103

Jang J, Narsilio GA, Santamarina JC, 2011. Hydraulic conductivity in spatially varying media—a pore-scale investigation. *Geophysical Journal International*, 184(3): 1167-1179. https://doi.org/10.1111/j.1365-246X.2010.04893.x

Kim S, Santamarina JC, 2015. Reactive fluid flow in CO_2 storage reservoirs: a 2-D pore network model study. *Greenhouse Gases: Science and Technology*, 5(4):462-473. https://doi.org/10.1002/ghg.1487

Kosugi K, 1996. Lognormal distribution model for unsaturated soil hydraulic properties. *Water Resources Research*, 32(9):2697-2703. https://doi.org/10.1029/96WR01776

Kosugi K, 1999. General model for unsaturated hydraulic conductivity for soils with lognormal pore-size distribution. *Soil Science Society of America Journal*, 63(2): 270-277. https://doi.org/10.2136/sssaj1999.03615995006300020003x

Laner D, Crest M, Scharff H, et al., 2012. A review of approaches for the long-term management of municipal solid waste landfills. *Waste Management*, 32(3):498-512. https://doi.org/10.1016/j.wasman.2011.11.010

Li YC, Tong X, Chen Y, et al., 2018. Non-monotonic piezocone dissipation curves of backfills in a soil-bentonite slurry trench cutoff wall. *Journal of Zhejiang University-SCIENCE A (Applied Physics & Engineering)*, 19(4): 277-288. https://doi.org/10.1631/jzus.A1700097

Mahabadi N, Dai S, Seol Y, et al., 2016. The water retention curve and relative permeability for gas production from hydrate-bearing sediments: pore-network model simulation. *Geochemistry, Geophysics, Geosystems*, 17(8):3099-3110. https://doi.org/10.1002/2016GC006372

Maitland GC, 2000. Oil and gas production. *Current Opinion in Colloid & Interface Science*, 5(5-6):301-311. https://doi.org/10.1016/S1359-0294(00)00069-8

Morrow NR, 1975. The effects of surface roughness on contact: angle with special reference to petroleum recovery. *Journal of Canadian Petroleum Technology*, 14(4):262-274. https://doi.org/10.2118/75-04-04

Mu DQ, Liu ZS, Huang C, et al., 2008. Determination of the

effective diffusion coefficient in porous media including Knudsen effects. *Microfluidics and Nanofluidics*, 4(3): 257-260.
https://doi.org/10.1007/s10404-007-0182-3

Ng CWW, Song D, Choi CE, et al., 2017. Impact mechanisms of granular and viscous flows on rigid and flexible barriers. *Canadian Geotechnical Journal*, 54(2):188-206.
https://doi.org/10.1139/cgj-2016-0128

Ng CWW, Choi CE, Koo RCH, et al., 2018. Dry granular flow interaction with dual-barrier systems. *Géotechnique*, 68(5):386-399.
https://doi.org/10.1680/jgeot.16.P.273

Öhrström P, Hamed Y, Persson M, et al., 2004. Characterizing unsaturated solute transport by simultaneous use of dye and bromide. *Journal of Hydrology*, 289(1-4):23-35.
https://doi.org/10.1016/j.jhydrol.2003.10.014

Phadnis HS, Santamarina JC, 2011. Bacteria in sediments: pore size effects. *Géotechnique Letters*, 1(4):91-93.
https://doi.org/10.1680/geolett.11.00008

Piovesan A, Achille C, Ameloot R, et al., 2019. Pore network model for permeability characterization of three-dimensionally-printed porous materials for passive microfluidics. *Physical Review E*, 99(3):033107.
https://doi.org/10.1103/PhysRevE.99.033107

Qin CZ, Hassanizadeh SM, 2015. Pore-network modeling of solute transport and biofilm growth in porous media. *Transport in Porous Media*, 110(3):345-367.
https://doi.org/10.1007/s11242-015-0546-1

Qin CZ, Hassanizadeh SM, Ebigbo A, 2016. Pore-scale network modeling of microbially induced calcium carbonate precipitation: insight into scale dependence of biogeochemical reaction rates. *Water Resources Research*, 52(11):8794-8810.
https://doi.org/10.1002/2016WR019128

Raoof A, Hassanizadeh SM, 2012. A new formulation for pore-network modeling of two-phase flow. *Water Resources Research*, 48(1):W01514.
https://doi.org/10.1029/2010WR010180

Raoof A, Spiers CJ, Hassanizadeh SM, 2011. Reactive pore scale modeling of porosity and permeability evolution in porous media. AGU Fall Meeting.

Ross PJ, Smettem KRJ, 2000. A simple treatment of physical nonequilibrium water flow in soils. *Soil Science Society of America Journal*, 64(6):1926-1930.
https://doi.org/10.2136/sssaj2000.6461926x

Sahimi M, 1993. Flow phenomena in rocks: from continuum models to fractals, percolation, cellular automata, and simulated annealing. *Reviews of Modern Physics*, 65(4): 1393-1534.
https://doi.org/10.1103/RevModPhys.65.1393

Scanziani A, Singh K, Bultreys T, et al., 2018. In situ characterization of immiscible three-phase flow at the pore scale for a water-wet carbonate rock. *Advances in Water Resources*, 121:446-455.
https://doi.org/10.1016/j.advwatres.2018.09.010

Shao W, Bogaard TA, Bakker M, et al., 2015. Quantification of the influence of preferential flow on slope stability using a numerical modelling approach. *Hydrology and Earth System Sciences*, 19(5):2197-2212.
https://doi.org/10.5194/hess-19-2197-2015

Šimůnek J, Jarvis NJ, van Genuchten MT, et al., 2003. Review and comparison of models for describing non-equilibrium and preferential flow and transport in the vadose zone. *Journal of Hydrology*, 272(1-4):14-35.
https://doi.org/10.1016/S0022-1694(02)00252-4

Singh K, Menke H, Andrew M, et al., 2017. Dynamics of snap-off and pore-filling events during two-phase fluid flow in permeable media. *Scientific Reports*, 7(1):5192.
https://doi.org/10.1038/s41598-017-05204-4

Sun X, Luo H, Soga K, 2018. A coupled thermal–hydraulic–mechanical–chemical (THMC) model for methane hydrate bearing sediments using COMSOL Multiphysics. *Journal of Zhejiang University-SCIENCE A (Applied Physics & Engineering)*, 19(8):600-623.
https://doi.org/10.1631/jzus.A1700464

Tuli A, Kosugi K, Hopmans JW, 2001. Simultaneous scaling of soil water retention and unsaturated hydraulic conductivity functions assuming lognormal pore-size distribution. *Advances in Water Resources*, 24(6):677-688.
https://doi.org/10.1016/S0309-1708(00)00070-1

van Dijk B, 2018. Design of suction foundations. *Journal of Zhejiang University-SCIENCE A (Applied Physics & Engineering)*, 19(8):579-599.
https://doi.org/10.1631/jzus.A1700465

van Genuchten MT, 1980. A closed-form equation for predicting the hydraulic conductivity of unsaturated soils. *Soil Science Society of America Journal*, 44(5):892-898.
https://doi.org/10.2136/sssaj1980.03615995004400050002x

Wang JQ, Zhao JF, Yang MJ, et al., 2015. Permeability of laboratory-formed porous media containing methane hydrate: observations using X-ray computed tomography and simulations with pore network models. *Fuel*, 145: 170-179.
https://doi.org/10.1016/j.fuel.2014.12.079

Weiler M, Flühler H, 2004. Inferring flow types from dye patterns in macroporous soils. *Geoderma*, 120(1-2):137-153.
https://doi.org/10.1016/j.geoderma.2003.08.014

Wu R, Zhu X, Liao Q, et al., 2010. Determination of oxygen effective diffusivity in porous gas diffusion layer using a three-dimensional pore network model. *Electrochimica Acta*, 55(24):7394-7403.
https://doi.org/10.1016/j.electacta.2010.07.018

Xiong QR, Baychev TG, Jivkov AP, 2016. Review of pore network modelling of porous media: experimental characterisations, network constructions and applications to reactive transport. *Journal of Contaminant Hydrology*, 192:101-117.
https://doi.org/10.1016/j.jconhyd.2016.07.002

Yan Z, Wang YZ, Yang ZX, et al., 2018. A strength degradation

model of saturated soft clay and its application in caisson breakwater. *Journal of Zhejiang University-SCIENCE A (Applied Physics & Engineering)*, 19(8):650-662. https://doi.org/10.1631/jzus.A1700461

Zhan LT, Xu H, Chen YM, et al., 2017a. Biochemical, hydrological and mechanical behaviors of high food waste content MSW landfill: preliminary findings from a large-scale experiment. *Waste Management*, 63:27-40. https://doi.org/10.1016/j.wasman.2017.03.008

Zhan LT, Li GY, Jiao WG, et al., 2017b. Field measurements of water storage capacity in a loess–gravel capillary barrier cover using rainfall simulation tests. *Canadian Geotechnical Journal*, 54(11):1523-1536. https://doi.org/10.1139/cgj-2016-0298

中文概要

题　目：孔隙特征对土体内部流动特性的影响——孔隙尺度的数值研究

目　的：研究土体内部的流动现象对岩土、农业及地质工程等领域具有重要意义。本文旨在探讨孔隙的平均直径、直径标准差、配位数及各向异性对土体内部水压、流量分布、流动模式及关键流动路径的影响，为评估土质屏障中的优势流动行为提供依据。

创新点：1. 在孔隙尺度分析孔隙特征对土体宏观渗透率及内部流动规律的影响；2. 评估多个孔隙特征参数（如孔隙的平均直径、直径标准差、配位数及三种孔隙直径分布形式）对土体内部优势流动行为的影响。

方　法：1. 将土体孔隙空间简化为由孔隙与吼道互相连接构成的球-杆模型，并通过改变孔隙和吼道的特征参数来描述复杂的孔隙结构；2. 利用孔隙网络模型得到单元体内部水压和流量分布情况，为计算土体固有渗透率和评估其流动特性提供基础数据；3. 基于击穿路径的概念，分析不同孔隙特征下土体内部流动的迂曲和非均匀程度；4. 通过引入吼道收缩系数，调整水平或竖直吼道直径大小，评估孔隙各向异性对流动规律的影响。

结　论：1. 土体的孔隙率和固有渗透率均随着孔隙直径平均值的增大、标准差的减小及配位数的增大而增大。2. 孔隙直径的变异系数（COV）越高，土体内部水压和流量的分布越不均匀；配位数的提高会削弱水压的局部化分布但会提高流量的不均匀程度。3.随着 COV 的提高，击穿路径变得更加曲折；当 COV 由 0 增加到 1.0 时，击穿路径的迂曲度由 1.00 增加到大约 1.71，击穿路径承担的流量占总流量的比值由 2.0%提高到 7.8%。4. 水平与竖直吼道直径比值的提高，也会导致击穿路径迂曲度的提高；水平与竖直固有渗透率的比值和水平与竖直吼道直径的比值呈双对数线性相关。

关键词：孔隙网络模型；固有渗透率；流动特性；孔隙特征